



**HAL**  
open science

## Geostatistical Analysis of Orographic Rainbands

Fabien Miniscloux, Jean Dominique Creutin, Sandrine Anquetin

► **To cite this version:**

Fabien Miniscloux, Jean Dominique Creutin, Sandrine Anquetin. Geostatistical Analysis of Orographic Rainbands. *Journal of Applied Meteorology*, 2001, 40 (11), pp.1835-1854. 10.1175/1520-0450(2001)0402.0.CO;2 . hal-03306582

**HAL Id: hal-03306582**

**<https://hal.science/hal-03306582>**

Submitted on 30 Jul 2021

**HAL** is a multi-disciplinary open access archive for the deposit and dissemination of scientific research documents, whether they are published or not. The documents may come from teaching and research institutions in France or abroad, or from public or private research centers.

L'archive ouverte pluridisciplinaire **HAL**, est destinée au dépôt et à la diffusion de documents scientifiques de niveau recherche, publiés ou non, émanant des établissements d'enseignement et de recherche français ou étrangers, des laboratoires publics ou privés.

## Geostatistical Analysis of Orographic Rainbands

FABIEN MINISCLOUX, JEAN DOMINIQUE CREUTIN, AND SANDRINE ANQUETIN

*Laboratoire d'études des Transferts en Hydrologie et Environnement, Observatoire des Sciences de l'Univers de Grenoble, Grenoble, France*

(Manuscript received 1 September 2000, in final form 3 March 2001)

### ABSTRACT

Based on weather radar detection, orographic rainbands parallel to wind direction may persist for several hours over a Mediterranean mountainous region prone to stable wind and humidity conditions. A statistical analysis shows that orographic rainbands are more active and more stable over the mountains than over the lower hills. By the mean of the range-time indicator technique, the northward advection velocity of the rain cells is deduced ( $60 \text{ km h}^{-1}$ ) and is slightly lower than the wind velocity ( $85 \text{ km h}^{-1}$ ) measured at the high-altitude weather station (Mont Aigoual, 1565 m above mean sea level). The detailed analysis highlights that the positioning of individual orographic cells in relation to the relief is not random: they are triggered by relief shoulders on their southeast flank. Their regular spacing (typically 15 km) is responsible for the general organization of the rainbands. Rain accumulations vary from 20 to over 100 mm day<sup>-1</sup> from the outside to the center of the rainbands.

### 1. Introduction

Mountain regions play a dominant role in the surface water balance of temperate areas. In the midlatitude climate of western Europe for instance, the French Alpine Isère River yields the same mean annual discharge as the Seine River in Paris but its watershed is almost 1 order of magnitude smaller. This difference is mainly caused by the massive excess of precipitation received by complex topography as compared with flat areas (about 1000 mm in the above example). Many issues ranging from integrated water management to climatic change detection and impact warrant an improvement in our understanding of the water cycle in these regions.

On a large scale, the low-level convergence of atmospheric moisture leading to the above-mentioned excess of precipitation is broadly related to two synoptic scenarios according to Cotton and Anthes (1989): 1) the genesis of mesoscale convective systems above and on the lee side of large mountain ranges, typical of summer conditions (Cotton et al. 1983), and 2) the modification of extratropical cyclones, more frequent under winter conditions (Browning 1980). At a local scale, various atmospheric processes producing orographic rain have been described in the literature (Smith 1979; Banta 1990), and, more recently, the paper of Barros and Kulligowski (1998) details the mutual contributions of the windward and leeward effects on the rainfall rate. The

lifting effect due to the presence of the slopes is the central process. Depending on the potential instability, orographic lifting induces either simple cloud development able to feed seeding rain from above (Bergeron 1965) or convection containing its own rain development.

The rainfall patterns resulting from these processes exhibit some regularities in their structure and in their positioning, reflecting the topography below. Climatological studies using rain gauge networks confirm that long-term rainfall accumulations (one month or more) linearly depend on the altitude (Hevesi et al. 1992a,b; Michaud et al. 1995), on the distance to topographic barriers (Schermerhorn 1967), or on the slope orientation (Daly et al. 1994). As far as short-term accumulations are concerned (a few days or less) the structure of orographic rain patterns is essentially analyzed for hydrologic applications. Reviews of some linear methods used for rain-field mapping are given, for example, in Creutin and Obled (1982). These methods are linear and assume spatial or temporal homogeneity [e.g., Chua and Bras (1982) used kriging, and Johnson and Hanson (1995) used principal component analysis]. Sophisticated nonlinear physically based models are also used to analyze orographic enhancement (Alpert 1986; Alpert and Shafir 1989; Barros and Lettenmaier 1993).

The difficulty in identifying local regularities of orographic rain fields partly stems from the well-known limitations of rain gauge networks, which includes drastic decrease in density with altitude, sensitivity to wind and snow conditions, and, until recently, nonsynchronous instrument clocks (Goodinson et al. 1989; Sevruk

Corresponding author address: Sandrine Anquetin, LTHE, BP 53, F-38041 Grenoble, Cedex 09, France.  
E-mail: sandrine.anquetin@hmg.inpg.fr

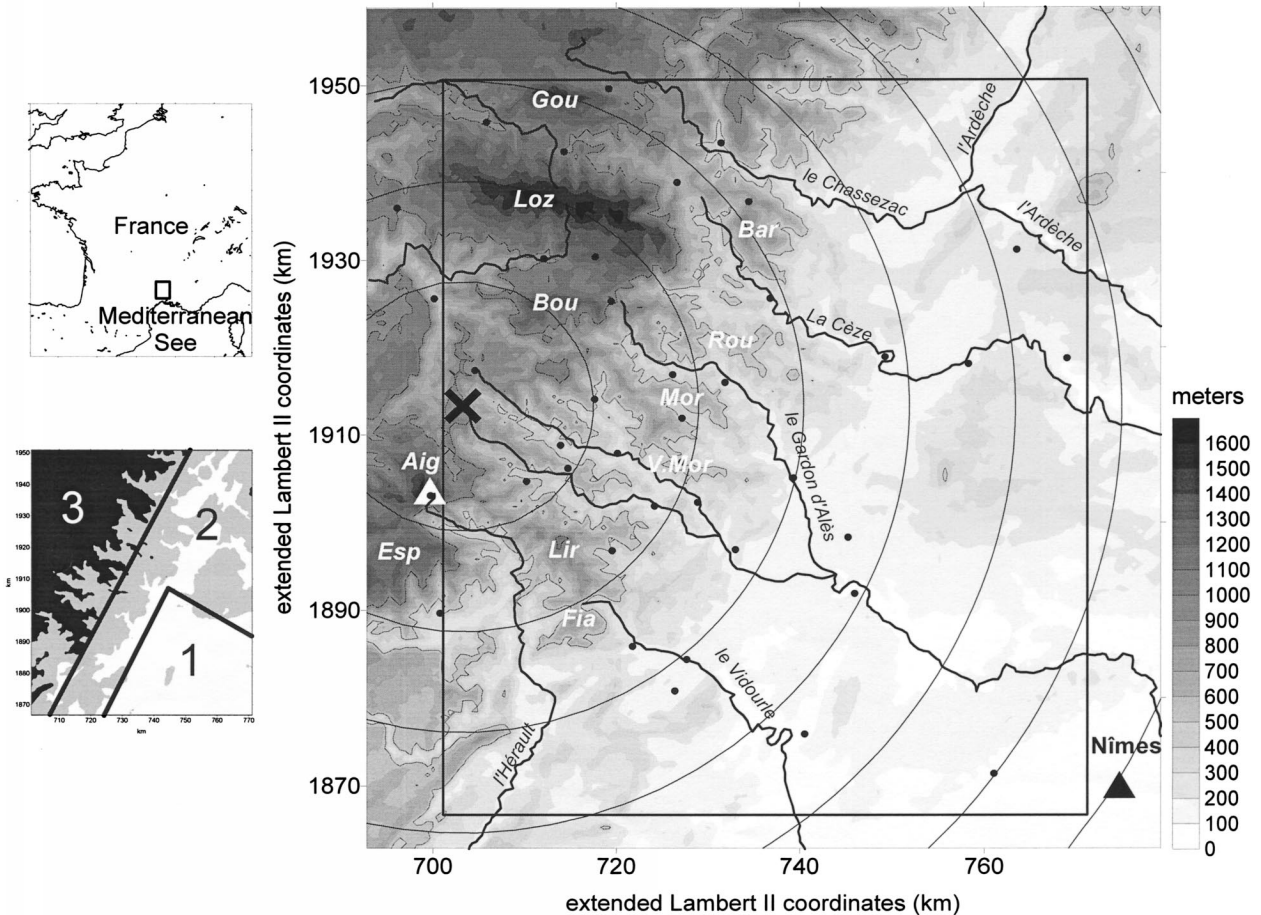


FIG. 1. Relief of the studied area. The DTM resolution is 75 m [Aig = Mont Aigoual (1565 m); Bar = Serre de Barre; Bou = Montagne du Bougès; Fia = Montagne de la Fiage; Gou = Montagne du Goulet; Lir = Montagne du Liron (922 m); Loz = Mont Lozère; Mor = Montagne de Mortissou; Rou = Montagne du Rouvergüe (695 m); V.Mor = Montagne de la Vieille Morte (920 m); the radar site (cross); the weather stations of Mont Aigoual and Nîmes (triangles); and 42 rain gauge stations (dots)]. On the left side are shown the general location in Europe (upper box) and the three topographic sectors.

and Klemm 1989). Weather detection by radar constitutes an alternative method even if the deployment of radar networks in complex terrain is still rare. The main reason for the limited number of radars is because radar assessment of rainfall in mountainous regions is significantly influenced by the orography itself (Joss and Waldvogel 1990). Until recently, these difficulties restricted the use of radar data of mountainous areas to the detailed studies of orographic-induced meteorological mechanisms (Hill et al. 1981) and discouraged their use on a statistical basis (Alpert and Shafir 1989; Harimaya and Tobizuka 1988). Nevertheless, radar probably offers a unique opportunity to explore orographic rain structure as was done for nonorographic rain in earlier work by Austin and Houze (1972), who classified rainstorms; Zawadski (1973) or Gupta and Waymire (1979), who analyzed the statistical structure of rain fields; and Lovejoy and Mandelbrot (1985) or Kumar and Foufoula (1993), who studied multiscaling of rainfall fields.

The current study investigates the statistical properties

of selected orographic rain fields in a mountainous region of Mediterranean Europe. In section 2, the Cévennes 1986–88 hydrometeorological experiment is shown to provide a reliable weather radar database. In section 3, a selection of 154 panoramic radar pictures [plan position indicator (PPI) scans] has been made according to stable wind conditions and in the absence of moving rain clusters. Statistical tools are then defined and applied to analyze quantitatively these selected orographic rain fields in terms of space structure, location with regard to topography, and dynamics (sections 4–6).

## 2. Dataset used

The Cévennes region is situated southeast of the Massif Central, the V-shaped Hercynian mountain range of the central part of France (85 000 km<sup>2</sup>; i.e., one-sixth of the country area). This relief is a southeasterly facing slope starting from the Mediterranean shore and the Rhône Valley. The altitude of the mountain range varies

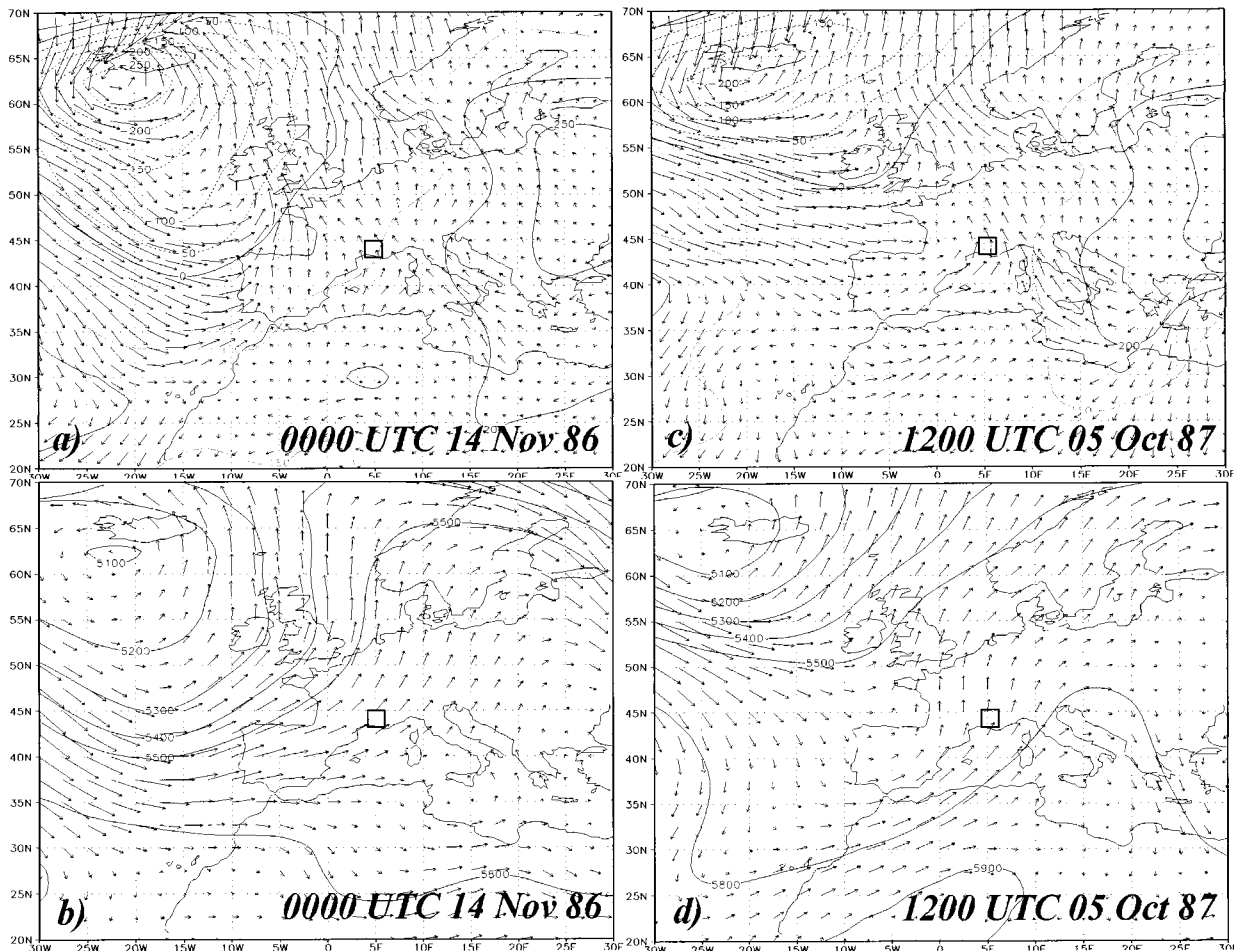


FIG. 2. The 1000-hPa geopotential height with wind at 10 m for (a) 0000 UTC 14 Nov 1986 and (c) 1200 UTC 05 Oct 1987; 500-hPa geopotential height and wind for (b) 0000 UTC 14 Nov 1986 and (d) 1200 UTC 05 Oct 1987. Data extracted from National Center for Atmospheric Research–National Centers for Environmental Prediction reanalysis.

from sea level up to 1500 m in roughly 30 km (i.e., a slope of over 5%). This hilly mass is dissected by deep (500-m depth) and narrow (10-km width) valleys oriented NW–SE (Fig. 1). According to elevation contours, three sectors can be identified: 1) a terrace around the city of Nîmes (below 200 m), 2) a hilly sector (between 200 and 500 m), and 3) a mountainous sector (above 500 m).

Like other Mediterranean mountain ridges and particularly in the autumn, the Cévennes region experiences prolonged rain events that are able to produce catastrophic floods over a wide range of river basin sizes (100–3000 km<sup>2</sup>). The meteorological situation associated with these rainfall events, commonly one to two days of almost continuous rain, is well understood and is briefly described.

Steady precipitation is formed by the presence of warm, moist air coming from the Mediterranean Sea. This southward-oriented flux is associated with an eastward-moving, upper-level trough reaching the French Atlantic coast. Figure 2 displays the geopotential and

wind fields for the two rain events used in this paper. In Figs. 2a and 2c, a 976-hPa surface low is located near Iceland and is associated with one or several cold fronts extending from England to Portugal (FO and FO' on Fig. 3). The front progression is slowed by the presence of an anticyclonic system over Russia. At ground level, the south of France is influenced by a south-southeasterly flow. The 500-hPa map (Figs. 2b,d) shows a deep trough of low pressure over the Atlantic. A ridge extending from the Mediterranean to Scandinavia is associated with the continental high and induces a clockwise curvature in the wind field over eastern Europe. Cosma et al. (2001) further detail the synoptic situation with their simulated soundings at Nîmes. These soundings reveal a stable upstream flow with an average moisture of 75% in the lower layers of the atmosphere (below 5000 m), as confirmed by the weather station records (see Fig. 7 below).

The Cévennes 1986–88 experiment took place during three consecutive autumns. The meteorological operational network that provided rain and wind measure-

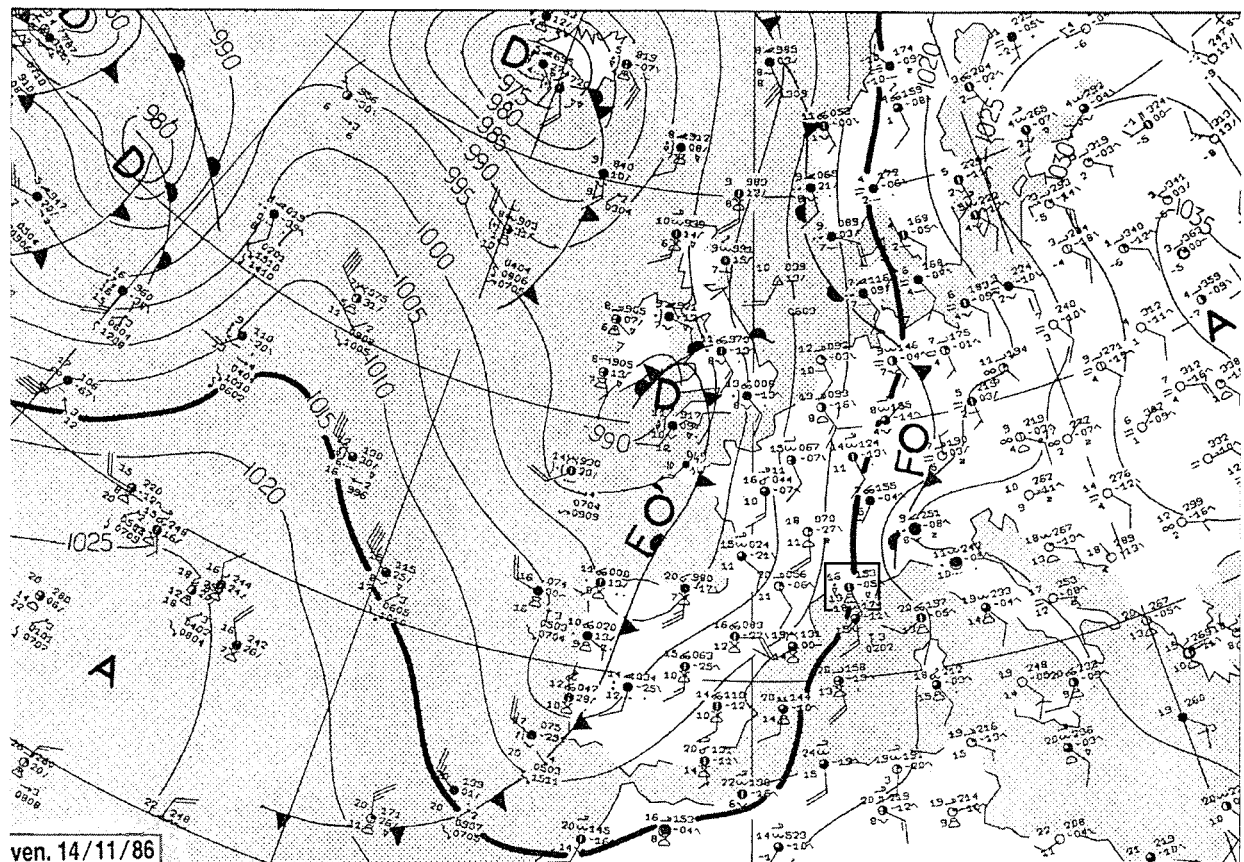


FIG. 3. Surface weather map adapted from the French national weather service (Météo-France) analyses, 1200 UTC 14 Nov 1986.

ments at ground level was complemented by a mobile weather radar. Almost 150 h of data were recorded, which resulted in more than 1000 mm of total accumulated rainfall at some gauge locations. They corresponded to four well-organized cyclonic perturbations that were properly forecast, which provided enough lead time for the operating teams to join the radar site. Prolonged and widespread rain events were associated with these perturbations.

The mobile S-band "Anatol" radar used during the experiment is characterized by a 4-m antenna dish, that is, a  $1.8^\circ$  half-power beam, a 250-kW peak power, and a  $2\text{-}\mu\text{s}$  pulse duration (Pointin et al. 1988). To survey three watersheds covering approximately 5000 km<sup>2</sup>, the radar was deployed near the village of Barre des Cévennes at an altitude of 1030 m (Fig. 1). The advantage of such positioning over the traditional valley siting is that it permits a better use of the low-elevation PPI pictures with fewer blocked sectors. The three main drawbacks are the presence of the bright band at short range, the difficulty in seeing the rain below the site, and the ground clutter produced by the sidelobes of the antenna at relatively far ranges. For this last point, the siting of the radar far enough from the edge of a small plateau significantly limited the propagation of sidelobes. The Anatol radar operated in PPI mode, recording

sequentially, each 8 min, two panoramic pictures at two elevation angles of about  $1.1^\circ$  and  $3.1^\circ$ . Because the radar was manually operated, changing the recording tape, fitting range–height indicator scans in between, or merely making manipulation mistakes meant that the pace of data acquisition at the rate of one picture each 4 min was not always rigorously maintained. The details of the radar data processing are given in Andrieu et al. (1997) and are summarized below.

A ground-clutter map was derived from clear-air pictures according to a 20-dBZ threshold. The beam-blockage correction factors of the elevation angles in operation were mapped after a digital terrain model (DTM) with a resolution of 1 km. The method used to reduce the brightband effect and to compensate for partial beam filling relies on the identification of vertical profiles of reflectivity (VPR). Over the studied area, hourly mean VPRs were identified using an inverse method (Andrieu and Creutin 1995). The reflectivity  $Z$  was converted into rainfall rate  $R$  according to a power-law relationship with a 1.38 exponent derived from the disdrometer of Joss–Waldvogel type used during the experiment (Creutin et al. 1997). The stability of the radar constant was checked in reference to marked ground detection. The absolute calibration of the radar was validated using a 42-rain gauge network (Andrieu et al. 1997). The cor-

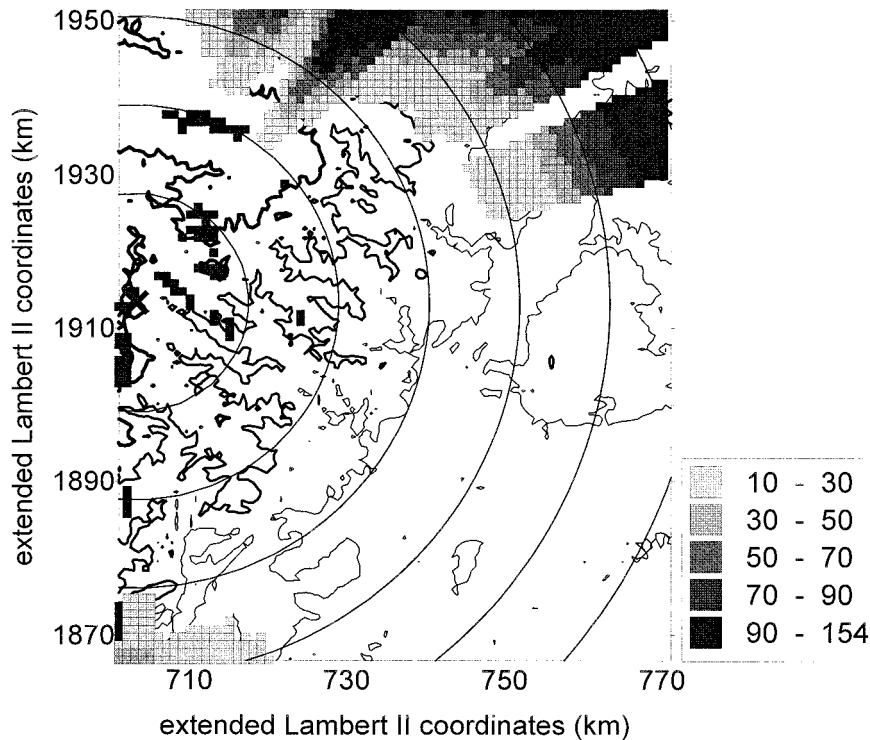


FIG. 4. Number of missing data for the 154 radar pictures in each radar bin after processing the ground clutter, the beam blockage, the vertical profile of reflectivity effect, and some residual echoes. The contour lines relate the altitudes of 200, 500, and 1000 m.

rections were applied to reflectivity maps according to a simple set of rules: 1) the applied correction factors must not exceed 2.5 and 2) the lowest elevation angle is always preferable. For these rules, Fig. 4 displays the number of unavailable measurements over the study period. The northern part of the study area beyond Mont Lozère and less extensively the southern part of the area beyond Mont Aigoual are affected by the combined effect of beam blocking and partial beam filling. Sets of ground-cluttered pixels are permanently unavailable on the mountain flanks facing the radar. Despite the care taken to eliminate the ground clutter, some clutter was detected when using range-time indicators (RTI) for showing variations of rain patterns in time. These nine pixels with more than 50% of the values larger than  $15 \text{ mm h}^{-1}$  were removed.

### 3. Description of orographic rainbands

The analysis of the radar pictures of the Cévennes 1986–88 experiment shows the coexistence of dynamic and static components in the rain fields. Different kinds of moving rain patterns, which are not studied in this paper, are presented in Fig. 5 to illustrate the dynamic component observed during the experiment. Associated with the passing of a cold front, eastward-moving rainbands exhibit a massive elongated shape (Fig. 5a). Known to be located in the warm sector of the distur-

bance, northward-moving patterns of organized convection have varied shapes ranging from compact (Fig. 5b) to narrow (Figs. 5c,d) bands oriented roughly perpendicularly to the flux. These types of rain patterns are well documented in the literature as organized convection and are related to the intrinsic instability of cyclonic air masses (Austin and Houze 1972; Cotton and Anthes 1989). It has given rise to a variety of stochastic-dynamic rainfall models (Amorocho and Wu 1977; Gupta and Waymire 1979; Smith and Krajewski 1987).

Besides this dynamic component, a static component is also observed. Its analysis is the focus of this paper. The static component is made of rainbands confined to the mountainous sectors and parallel to wind direction. They result from the triggering of warm-sector instability by the relief, and, in that sense, the word orographic is proposed to designate these bands. This assertion does not preclude a possible role of orography on the dynamic component of the rain fields. Providing evidence on the triggering or enhancement of moving rainbands by the relief is probably more delicate and in any case is impossible in this study given the extent of the covered domain. Orographic rainbands are not easily shown or analyzed given that 1) their usual rain intensities ( $<10 \text{ mm h}^{-1}$ ) are drowned by the intensities of the moving rain patterns (several tens of millimeters per hour), 2) their complex structure is not captured well by the current density of rain gauge networks (Fig. 6),

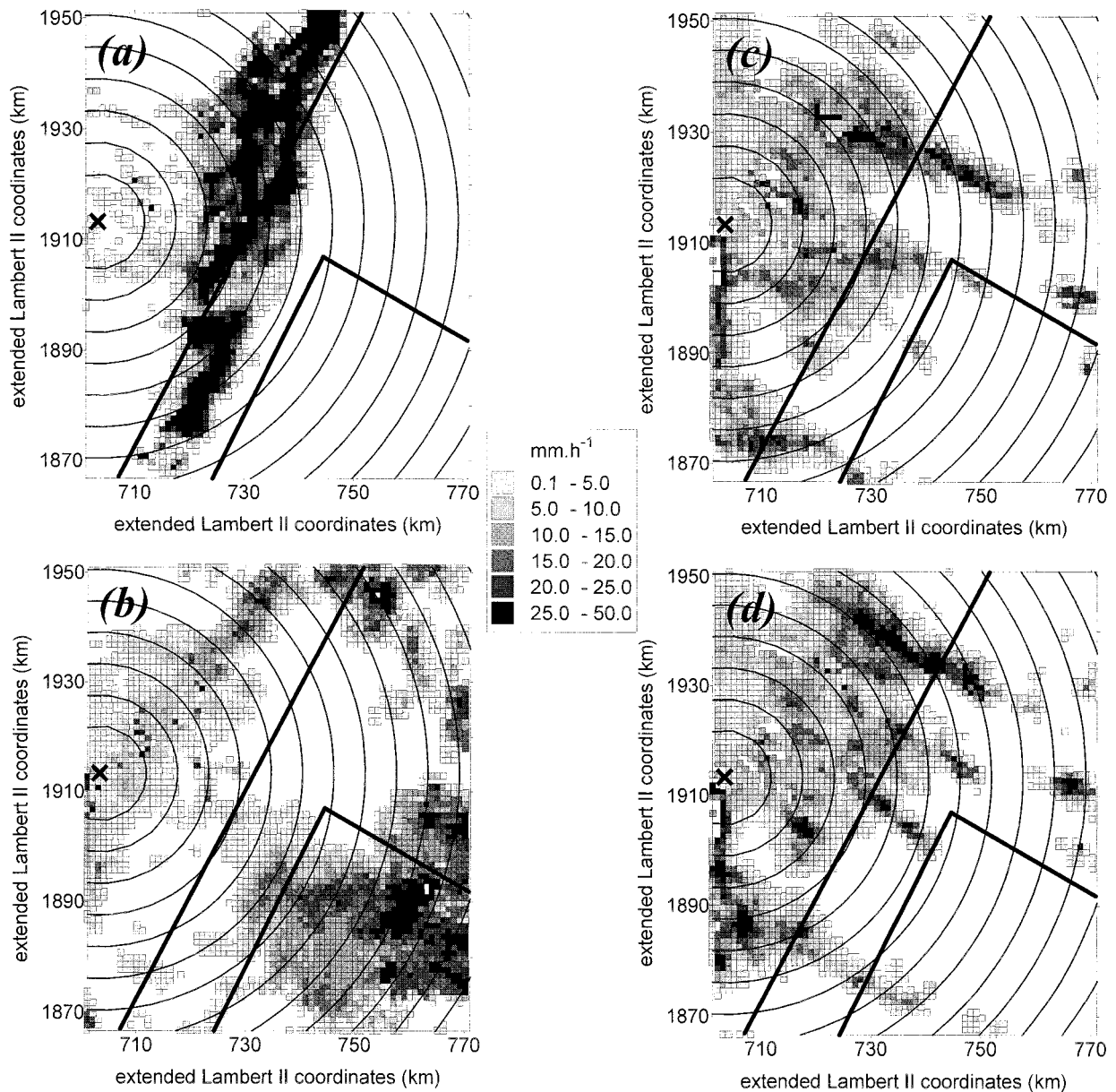


FIG. 5. Processed radar pictures featuring the dynamic rain-field component during observed events: (a) 0826 UTC 11 Oct 1988, eastward-moving band associated with the cold front; (b) 0022 UTC 5 Oct 1987, northward-moving rainband in the warm sector of the perturbation; and (c) and (d) 2343 UTC 5 Oct 1987 and 2353 UTC 5 Oct 1987, narrow northward-moving rainbands at two successive instants indicating an approximate advection velocity of  $60 \text{ km h}^{-1}$ .

and 3) their patterns depend on the wind conditions, which vary in time. Among the almost 150 recorded hours of the Cévennes 1986–88 experiment, approximately 20 h of observation were selected as representing only orographic rainbands. The selection relies on two simple observation features related to wind direction and rain patterns: 1) a sustained and almost saturated wind blows for several hours around a constant direction, and 2) the rain patterns are confined to the relief zone and remain steady at the scale of the observed area.

A sequence of 16 continuous hours on 14 November 1986 makes up the prevailing part of the sample. The four remaining hours come from 5 October 1987. In total, 154 “instantaneous” radar pictures were selected. Figure 7 shows that, for the selected rain hours, the wind at Mont Aigoual (1565 m) and at Nîmes (39 m) was steadily blowing from the south with a velocity larger than  $20 \text{ m s}^{-1}$  and the air humidity at the surface at Nîmes was almost saturated. Figures 8a and 8b display two selected fields from 5 October 1987 separated by a time interval of 8 min. The rainbands are static and

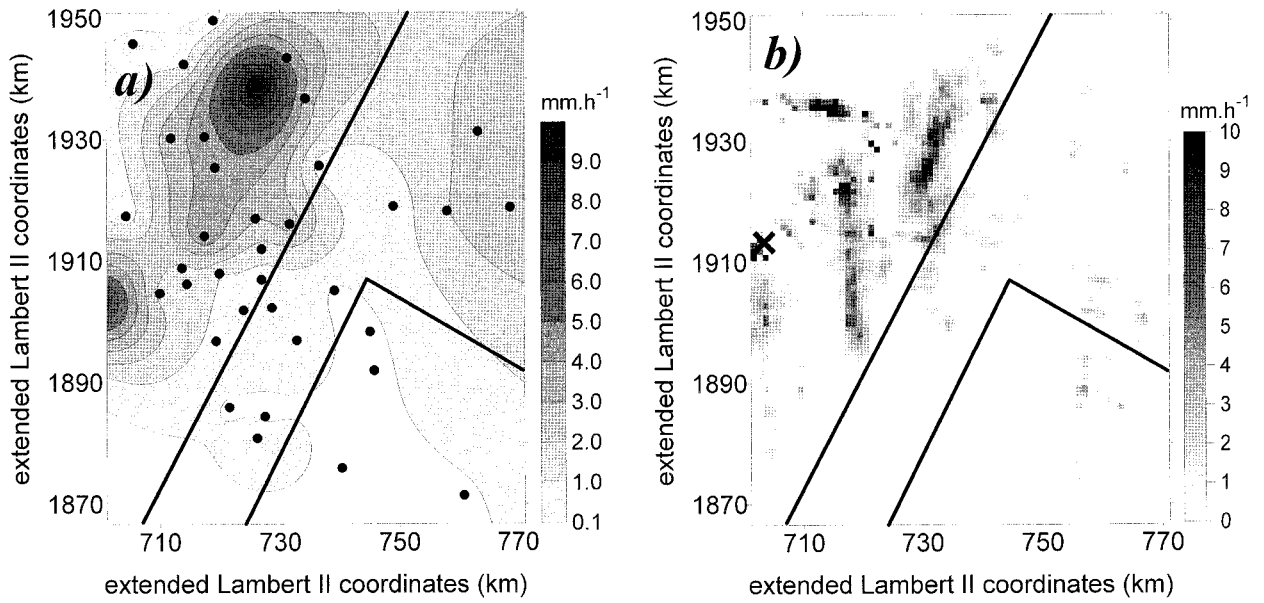


FIG. 6. Hourly rainfall intensities on 14 Nov 1986 from 1400 to 1500 UTC: (a) kriging of 42 rain gauge readings and (b) averaging radar pictures.

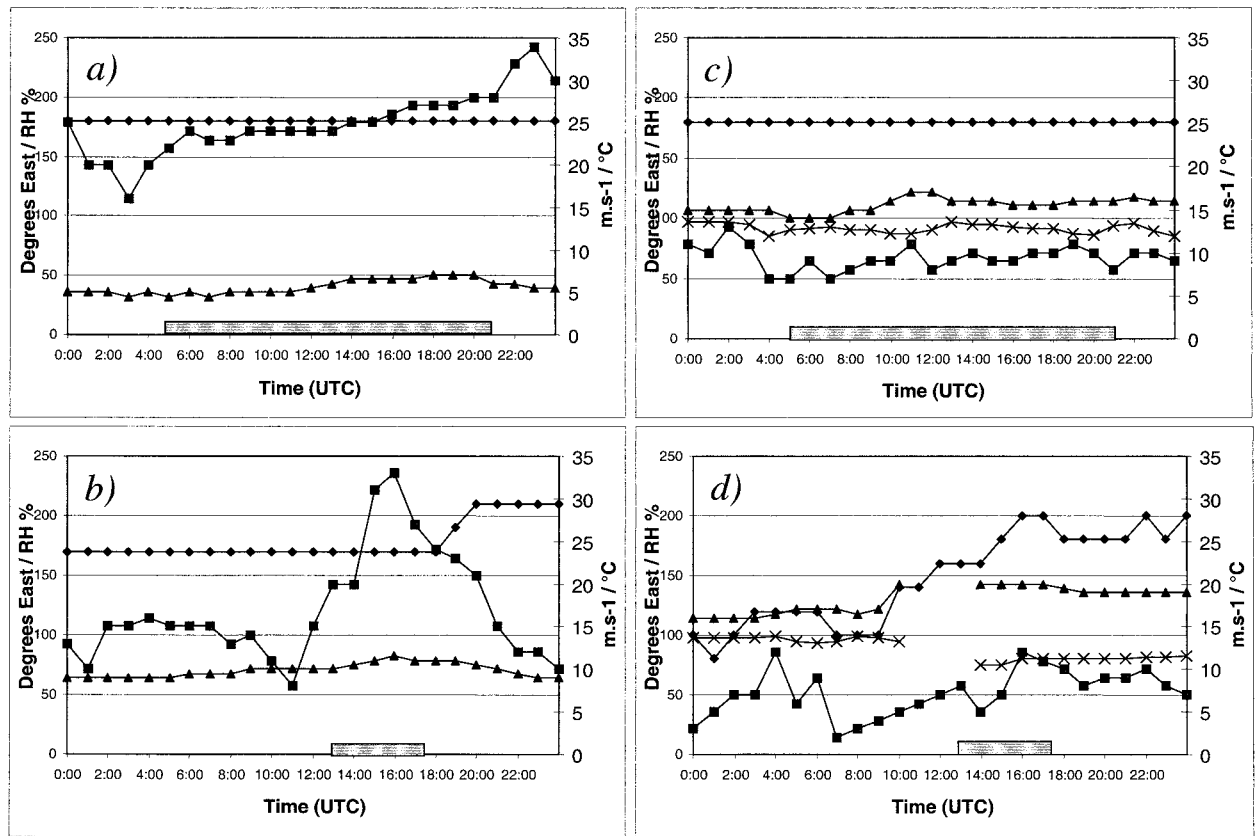


FIG. 7. Time records of wind direction ( $\blacklozenge$ ), wind velocity ( $\blacksquare$ ), temperature ( $\blacktriangle$ ), and relative humidity (RH) ( $\times$ ) at the Mont Aigoual weather station (1565 m) on (a) 14 Nov 1986 and (b) 5 Oct 1987 and at the Nîmes weather station (39 m) on (c) 14 Nov 1986 and (d) 5 Oct 1987. The studied periods are indicated along the time axis.

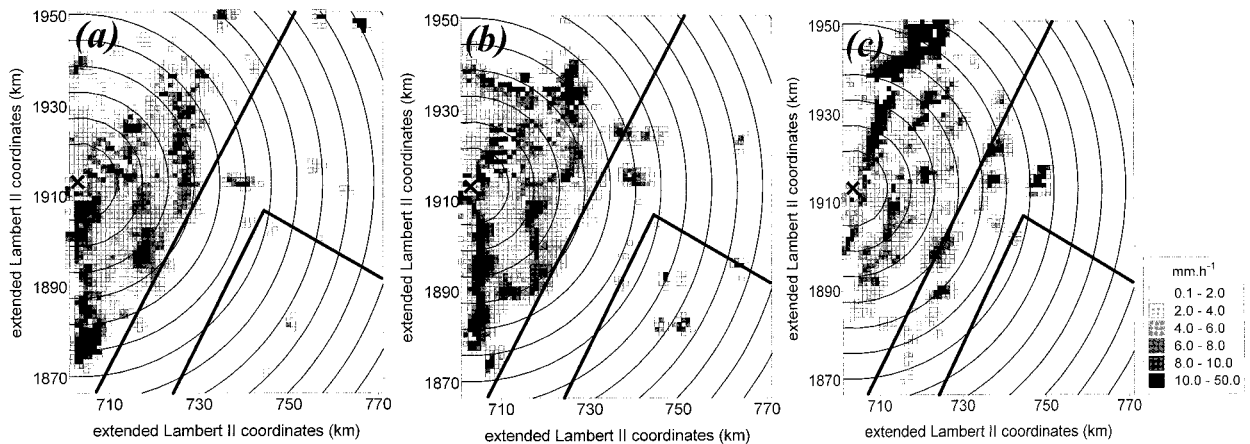


FIG. 8. Processed radar pictures featuring the static component of the rain fields in the warm sector on 5 Oct 1987: (a) 1456 and (b) 1504 UTC radar pictures with orographic rainbands resulting from an N-170°E wind and (c) 1821 UTC with the same bands when the generating flux turned from N-170°E to N-210°E.

oriented north–south even if their shape and internal structure slightly change over time. The governing role of the wind direction on the band orientation is illustrated in Fig. 8c. As indicated in Fig. 7b, the wind in the high-altitude weather station (1565 m) turned from N-170°E to N-210°E at around 1800 UTC, inducing the band rotation observed at 1821 UTC. Inside the bands the rain intensity fluctuates, with typically more than 10 mm h<sup>-1</sup> in individual cells.

For each hour, a mean vertical profile of reflectivity was identified over the studied area (section 2). The 20 profiles corresponding to the selected periods of orographic rain are plotted in Fig. 9. The highest radar echoes are roughly 1.5–2 km above the mountain tops, which are 1.5 km high. No brightband effect is present except for the last hour of 5 October 1987. Thus the icing level is above the echo tops, which is consistent with the temperature of 5° and 10°C measured at Mont Aigoual (Figs. 7a,b). The absence of low-level reinforcement or erosion on these profiles excludes, respectively, significant Bergeron's seeder–feeder effect and under-cloud evaporation. The above information leads to the assumption of shallow warm convection. If rain fields reflect topographic features on scales that depend on rain-producing processes, such a low vertical development should lead to rain-field structures that reflect small topographic features.

According to the above qualitative description, the selected orographic rain fields are made of stable alignments of rain cells triggered by specific relief features. To confirm this view quantitatively, this study offers a geostatistical analysis of these observations. It successively answers the questions of 1) persistence in space of orographic bands, 2) localization of rain cells with respect to the relief, and 3) dynamics of the rain cells.

To our best knowledge, this kind of static rain pattern is less documented than the dynamic one and has an

important effect on the hydrological processes at local scale, even if its associated rainfall is lower (Barros and Kuligowski 1998). Because of the better means of the atmospheric observations, the main characteristics of the rain over complex terrain have been identified (Barros and Kuligowski 1998; Bougeault et al. 2001). In a recent paper (Cosma et al. 2001), these kinds of rainbands have been successfully simulated with a nonhydrostatic atmospheric model. Idealized simulations show that the banded structure of the precipitation patterns results from the combination of several mechanisms involving flow dynamics above and around small-scale topographical disturbances such as orographic lifting, vertically propagating mountain waves, and leeside convergence.

Orographic rainbands deserve to be studied for at least two reasons, as follows.

- 1) They constitute a simple example of rain pattern related to the topography; their reproducibility and their sensitivity to the flux conditions can probably be tested further with other radar datasets and numerical meteorological models.
- 2) Their impact on the rain climate of mountainous areas is probably strong despite their modest intensity; if this static component of the rain field is present during the total duration of this kind of rain event, typically lasting 2–3 days, orographic rainbands are able to bring substantial accumulations of more than 100 mm day<sup>-1</sup> distributed in space in a variable manner.

#### 4. Distribution of orographic rain in space

If the alignments of rain cells observed during the selected periods are stable in time, the corresponding rain fields should be statistically second-order nonstationary in space. The two first-direct moments should

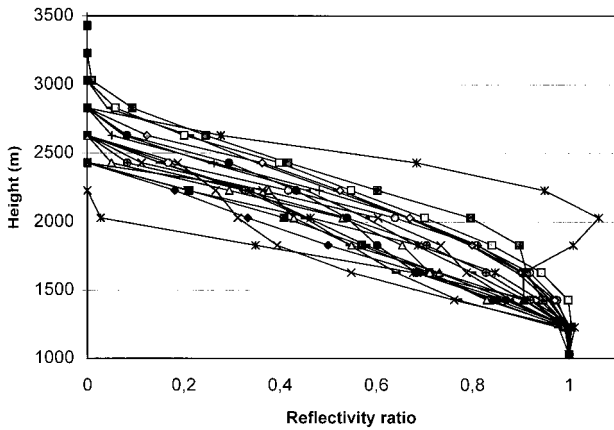


FIG. 9. Mean hourly VPR corresponding to the 20 selected hours.

be space dependent; the structure function should be nonisotropic and should exhibit trend effects.

In the following we consider the instantaneous rainfall rate as being a random function observed over a study domain  $D$  and a finite set of  $N$  realizations in time. We denote  $R(\mathbf{x}, i)$  the rainfall rate at  $\mathbf{x} = (x, y)$  for the  $i$ th realizations. We analyze successively the mean, the variance, and the covariance.

a. Mean and variance fields

Let  $m_R(\mathbf{x})$  and  $s_R^2(\mathbf{x})$  be respectively the sample estimates of the mean  $E[R(\mathbf{x})]$  and the variance  $E\{R(\mathbf{x}) - E[R(\mathbf{x})]\}^2$  of the random function  $R$  (rain rate) at point  $\mathbf{x}$ . They can be computed at each radar grid point  $\mathbf{x}_g$  over  $N = 154$  radar pictures as

$$em_R(\mathbf{x}_g) = \frac{1}{N} \sum_{i=1}^N R(\mathbf{x}_g, i) \quad \text{and} \quad (1)$$

$$s_R^2(\mathbf{x}_g) = \frac{1}{N} \sum_{i=1}^N [R(\mathbf{x}_g, i) - m_R(\mathbf{x}_g)]^2, \quad (2)$$

where  $i$  indexes the successive rain fields.

The mean and variance maps presented in Fig. 10 suggest the following comments.

- 1) Five north–south-oriented corridors dominate the rain-field statistics. These corridors are marked by coherent fluctuations in space of means and variances. Their N–S axes are approximately 15 km apart (at  $x = 705, 718, 730, 745,$  and  $760$  km Lambert II coordinate).
- 2) The flat Nîmes area (sector 1) is almost free of any mean and variance signature. Rain activity is strictly limited to the mountain area during the selected hours.
- 3) The three west corridors correspond to sector 3. They exhibit higher means and narrower shapes. The mean rain intensity can vary along the longitude from less than 1 to more than 8 mm h<sup>-1</sup> in less than 10 km (rain accumulations of up to 80 mm for the November 1986 case). According to the variance map, rain fluctuations show several marked peaks along each band, one peak being systematically at the southern edge of the band. This peak matches the first marked relief met by the wind flux. In Fig. 10, these mountains [Montagne de l’Espérou (Esp), Montagne du Liron (Lir), and Montagne de la Vieille Morte (V. Mor)] are shown and are approximately 1000 m high.
- 4) The two remaining east corridors belonging to the hilly area (sector 2) have lower means (<5 mm h<sup>-1</sup>) and higher variances (>100 mm<sup>2</sup> h<sup>-2</sup>). In other

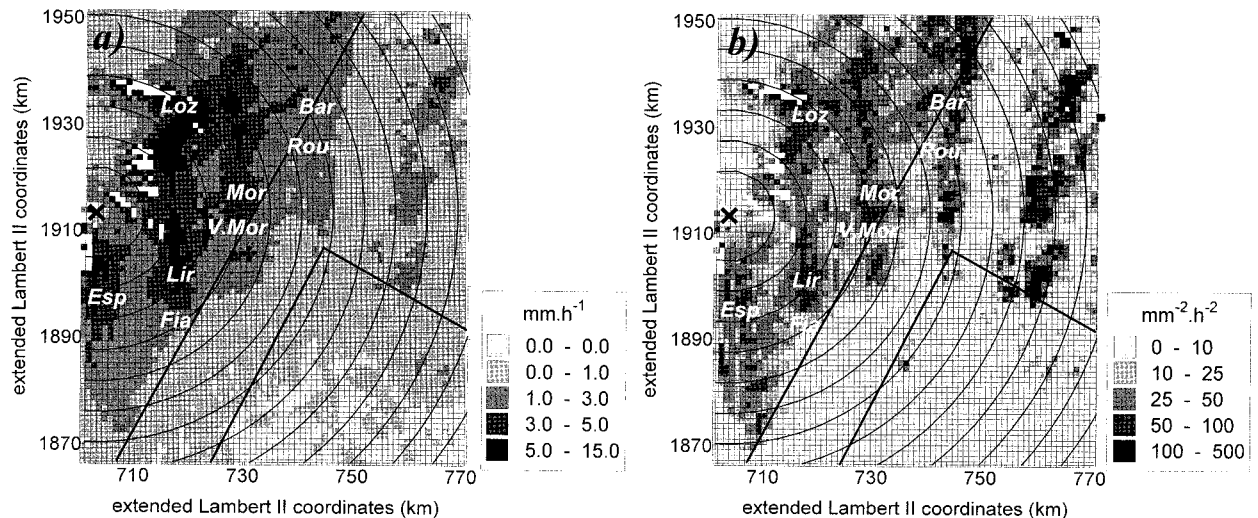


FIG. 10. (a) Mean rainfall rate; (b) variance of the rainfall rate. White pixels denote missing data.

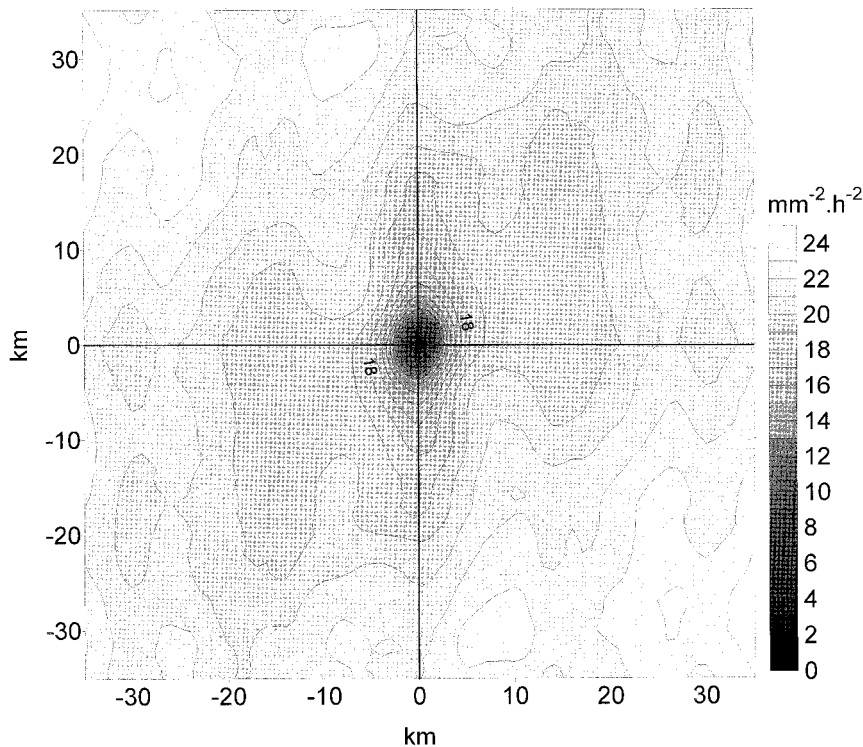


FIG. 11. Two-dimensional variogram function  $v_R(X, Y)$  obtained for the set of 154 selected pictures using a square window of  $70 \times 70 \text{ km}^2$ .

words, the rainbands are less productive and more variable in time in this area of lower altitude. In terms of shape, these bands are wider than the three others, probably because the topography is less pronounced here (less than 700 m high for the highest peaks).

- 5) The northern part of the study area has a more complex structure (beyond  $y = 1930 \text{ km}$  Lambert II coordinate). However, it must be kept in mind that the presence of Mont Lozère (Loz) renders this part of the radar picture unreliable because of beam blockage (Fig. 4). Nevertheless, the disturbance caused to the flow by the mountain produces NE–SW alignments of the mean and variance fields, establishing links between the N–S corridors (2–3 and 3–4).
- 6) The matching characteristics of the two maps confirm the relationship between mean and variance frequently observed in rain fields, although one can note that this relationship slightly changes from sector 2 to sector 3. The slope of the regression line computed using pixel data as individual points can be shown to vary from 0.25 (sector 2) to 0.50 (sector 3). This characterizes a nonstationary field.

In summary, the two first-direct moments of the selected rain fields are nonstationary in space. It is a first piece statistical evidence of the existence of static rain bands in stable wind flux conditions.

#### b. Structure function

Let  $\gamma(\mathbf{h})$  be the half mean square of the increments of the random function  $R$  over a geographic distance  $\mathbf{h}$ :

$$\gamma(\mathbf{h}) = \frac{1}{2}E[R(\mathbf{x}) - R(\mathbf{x} + \mathbf{h})]^2. \quad (3)$$

Written as such, the function  $\gamma$  only depends on the oriented distance  $\mathbf{h}$  and not on the location of the point  $\mathbf{x}$ . It is thus 1) possibly nonisotropic and 2) defined only for a stationary random function. This function is called a structure function or variogram (e.g., Gandin 1965; Matheron 1965).

It is always possible to compute a variogram under nonstationary conditions as in this study. When interpreting the results, it must be kept in mind that the variogram for short displacements  $\mathbf{h}$  is not sensitive to space variation of the mean, because the increments  $R(\mathbf{x}) - R(\mathbf{x} + \mathbf{h})$  filter out a constant, that is, the local mean level of the random function. The intrinsic field variability will then be captured well by the short distances of the variogram. At larger displacement  $\mathbf{h}$ , the space variation effect of the mean and the variance will dominate the variogram behavior.

The continuous sampling of radar data allows an estimation of the variogram  $\gamma(\mathbf{h})$  over a window of chosen size. Let us define  $X$  and  $Y$  as the relative coordinates of a point in a moving window of size  $[(-X_{\max}, X_{\max}), (-Y_{\max}, Y_{\max})]$ . Let  $(x_w, y_w)$  be the radar grid coordinates

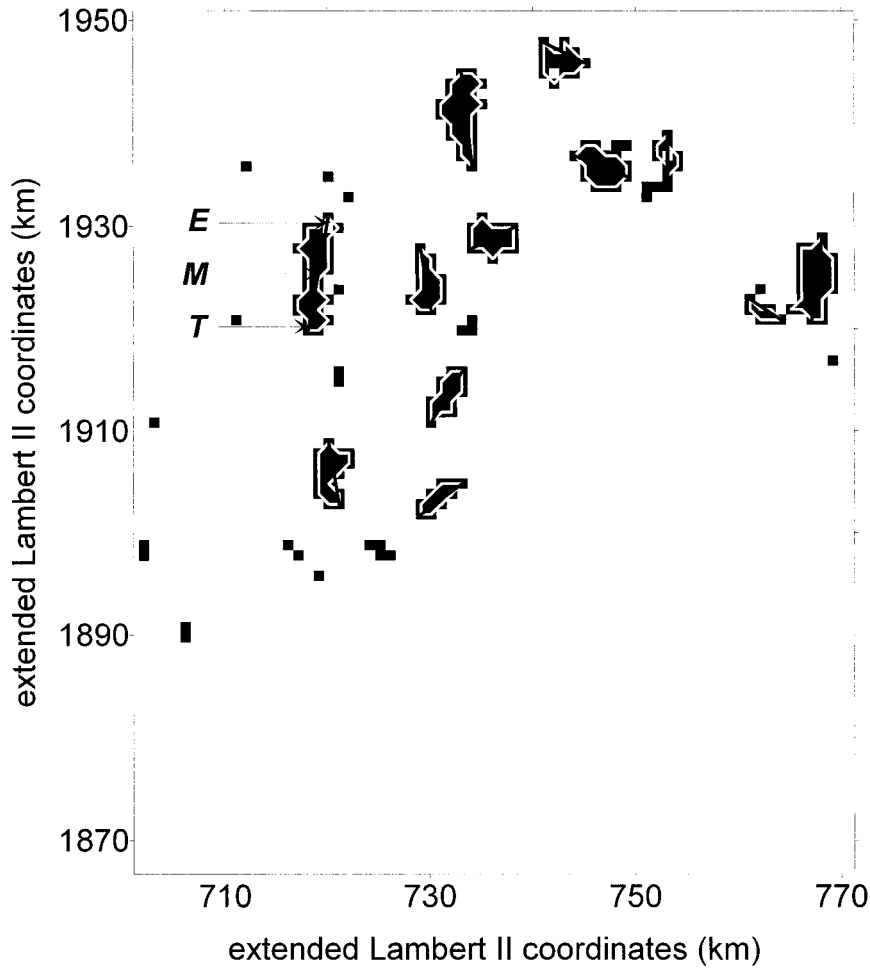


FIG. 12. Raincell identification for a given threshold  $\tau = 10 \text{ mm h}^{-1}$  at 0816 UTC 14 Nov 1986. Black pixels shows the threshold, and the white solid line embodies the cell contour. Morphometric features are pointed out: T is triggering point, E is end point, and M is major axis.

of the center of the window. The estimate  $v_R(X, Y)$  of the 2D variogram function  $\gamma(\mathbf{h})$  is expressed by

$$v_R(X, Y) = \frac{1}{2N_{x,y}N} \sum_{i=1}^N \sum_{w=1}^{N_{x,y}} \{R[(x_w, y_w), i] - R[(x_w + X, y_w + Y), i]\}^2, \tag{4}$$

where  $N_{x,y}$  is the number of available points when the window moves across the radar picture and  $N$  is the number of available observations. This 2D variogram

is more informative on the field anisotropy than the 1D variogram  $\gamma_R(h)$ , which is derived by integration of  $v_R(X, Y)$  at constant distances  $h = \|\mathbf{h}\|$ .

Figure 11 displays the resulting 2D variogram  $v_R(X, Y)$  on the  $70 \times 70 \text{ km}^2$ -sized window. The function  $v_R(X, Y)$  using a square expression [Eq. (4)] is symmetrical and could have been displayed within a smaller domain. Nevertheless, the presentation of the whole window ( $70 \times 70 \text{ km}^2$ ) is more readable. The corresponding 1D variogram (not presented here) can be fitted by a spherical model whose characteristics are

TABLE 1. The 16%, 50%, and 84% quantiles for the cumulative distribution functions of raincell surface and length for different rain-rate thresholds  $\tau$ . For a normal distribution, these three quantiles correspond to the median and plus or minus one standard deviation.

	2.5 mm h <sup>-1</sup>			10 mm h <sup>-1</sup>			15 mm h <sup>-1</sup>		
	16%	50%	84%	16%	50%	84%	16%	50%	84%
Surface (km <sup>2</sup> )	8	18	83	8	14	37	8	13	30
Length (km)	3.6	5.8	17.5	3.2	5	9.5	3.2	4.5	8.5

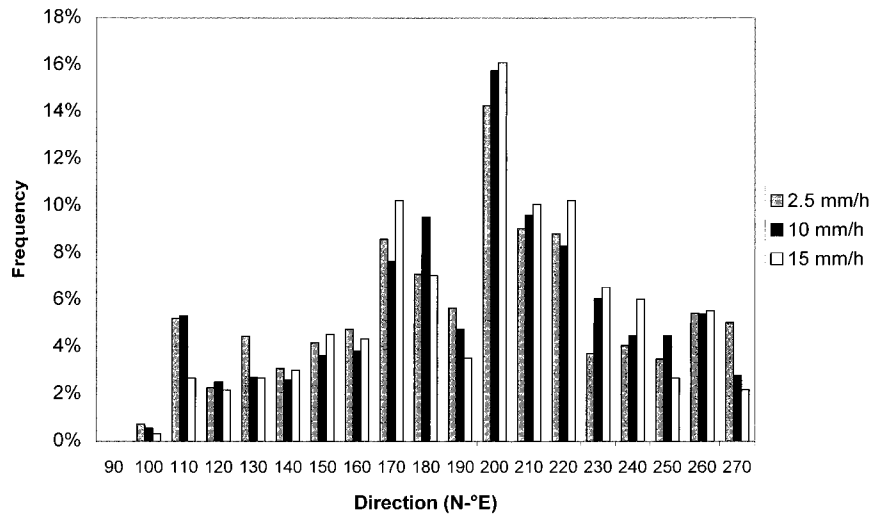


FIG. 13. Statistical distribution of the major axis orientation (in N-°E) of rain cells.

summarized by no nugget effect, a range of 7 km, and a sill of  $19 \text{ mm}^2 \text{ h}^{-2}$ . The following comments can be made.

- 1) At short range (less than 5 km) the 2D variogram is isotropic and without nugget effect. This last point is confirmed by the 1D variogram and is due to the integration of the small-scale rain variability by the radar beam. The intrinsic variability of the rain field is thus “smooth,” isotropic, and with a typical correlation length of about 5–7 km (taking  $12 \text{ mm}^2 \text{ h}^{-2}$  as a limit corresponding to 50% of explained variance). These features have been observed in other kinds of rain at comparable scales (e.g., Messaoud and Pointin 1990).
- 2) At longer range (more than 5 km), the 2D variogram shape becomes clearly nonisotropic. It reflects the trend of the mean at field scale. Within a range of 15 km, the elliptic shape of the variogram results from the typical size of the individual elements forming the rainbands: about 15 km northward and 5 km eastward. The longitudinal replication of this shape at 15 and 30 km is related to the typical spacing of the bands determined by the spacing of the triggering topographic elements. The SW–NE orientation of these different shapes probably comes from the mean slope of the relief around N-135°E.

This variogram analysis summarizes the main features of orographic rain organization in space from the level of the constitutive rain cells to the scale of the bands.

## 5. Distribution of rain cells in space

If rain cells are triggered by specific relief features, the underlying topography should statistically differ from the mean topography. In the following section, we consider a rain cell as a connected set of contiguous radar grid points  $\mathbf{x}_g$  for which the rain rate exceeds a

given threshold, that is,  $R(\mathbf{x}_g) \geq \tau$ , where  $\tau$  is the threshold ( $\text{mm h}^{-1}$ ).

### a. Raincell identification

The identification algorithm used consists of searching from a starting point above the threshold for the neighboring pixels that maximize the raincell contour (e.g., Rosenfeld 1969). The contours that contain less than a minimum number of pixels (six in this case) are not retained, so as to exclude cells that are too small. Figure 12 displays an example of cell identification showing that each field can include several rain cells. The total number of rain cells identified for the three thresholds  $\tau$  chosen to be 2.5, 10, and  $15 \text{ mm h}^{-1}$  was equal to 1746, 1072, and 596, respectively. For each cell, morphologic elements are determined such as the surface and the major axis, defined as the longest segment included in the contour (M in Fig. 12). During the selected periods, the wind blows from the south; the southern end of the major axis is thus supposed to be the triggering point of the rain cell (T in Fig. 12). Of course, this geometric definition is disputable from the point of view of the rain production processes. Nevertheless it is used here to define simply the origin of a common coordinate system that allows the combined analysis of all the rain cells.

The 16%, 50%, and 84% quantiles are listed in Table 1 for the length and the surface of rain cell distributions. The surface and major-axis-length distributions are strongly asymmetric, with median values of 13–18  $\text{km}^2$  and 5–6 km, respectively, which are almost threshold independent. This result confirms the strong anisotropy of the rain field detected by the variogram (a ratio of typically 3 between the major and the minor axis). The distribution of major-axis orientations presented in Fig. 13 is globally symmetric, with a median value of N-200°E independent of the threshold. Two submodes can

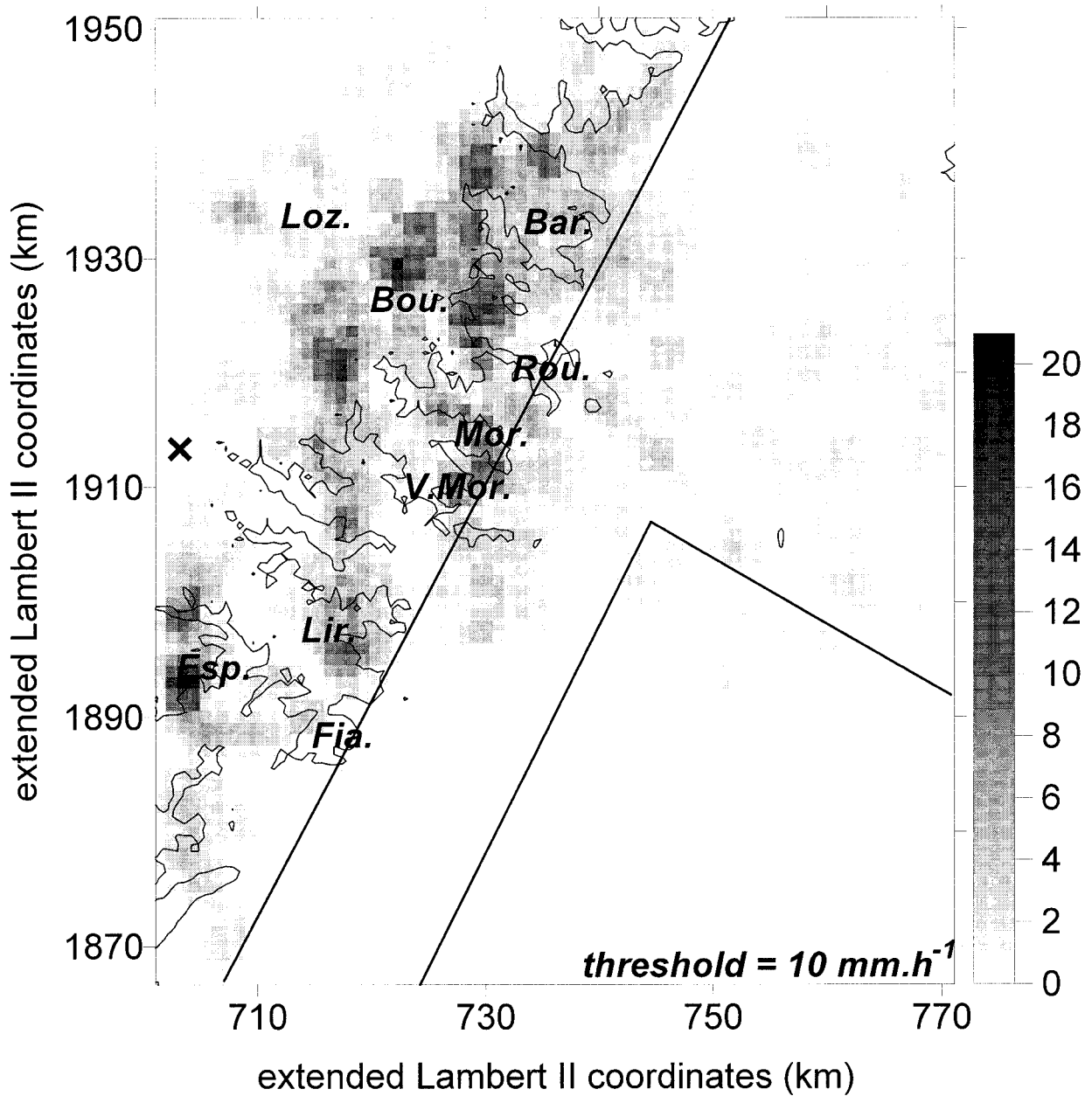


FIG. 14. Triggering point densities in a moving  $4 \times 4 \text{ km}^2$  window for a threshold  $\tau = 10 \text{ mm h}^{-1}$ . The relief contour line corresponds to 500 m high.

be identified: 1) N-S-oriented cells contributing to the corridors readable in Fig. 10, and 2) N-220°E-oriented cells responsible for the links denoted between these corridors. The two modes are certainly governed by the growing influence of the hill mass in deflecting the wind flux eastward when reaching the north of the study domain. In summary and concerning the threshold used, only the size distributions are affected, given that, of course, larger thresholds delineate smaller rain cells. Nevertheless, the conclusions derived having little dependence on the threshold, we restrict the following analysis to  $\tau = 10 \text{ mm h}^{-1}$ .

*b. Distribution in space*

Rain cell distribution in space and its relationship to the underlying topography can be analyzed either in the studied domain coordinate system (Eulerian) or with respect to the position of rain cells (Lagrangian). Both approaches are proposed in the following.

Figure 14 displays a map of cell triggering-point densities over the studied domain. The number of triggering points is computed in a moving window of  $4 \times 4 \text{ km}^2$  centered on each radar grid element. The corridors identified with the mean and variance maps (Fig. 10) are again

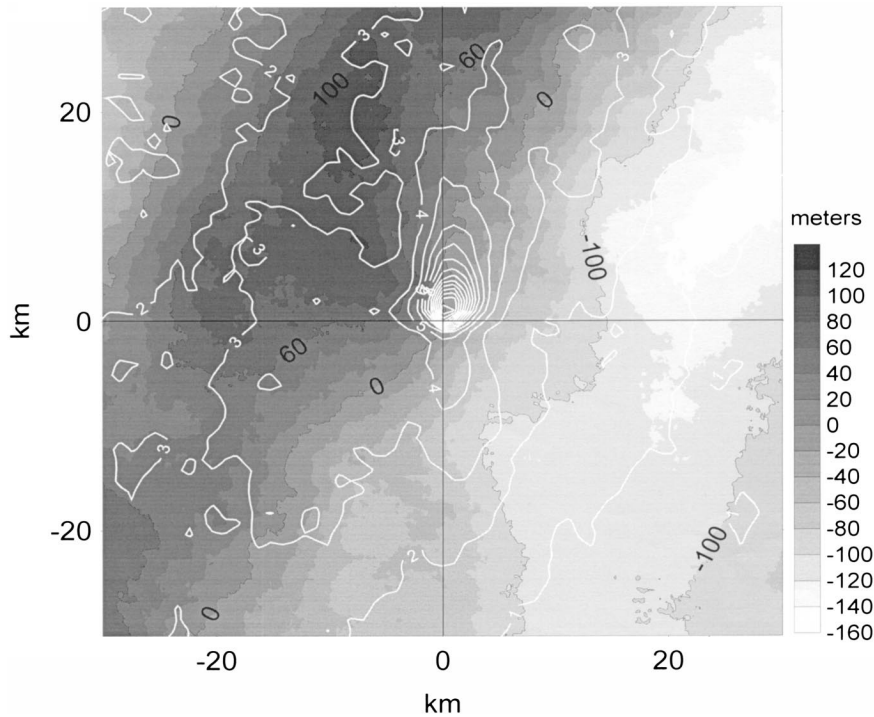


FIG. 15. Mean statistical rain field (white contours: mm) and corresponding mean underlying topographic deviation (gray scale) from the mean relief centered on the triggering point of identified rain cells.

present in this map, which brings the following information.

- 1) The western corridors belonging to sector 3 are significantly more active in terms of producing rain cells above  $10 \text{ mm h}^{-1}$  than are the eastern corridors. The proportion of cell triggering per corridor from west to east is respectively of 20%, 25%, 30%, 15%, and 10%. Thus the third-eastward rainy corridor triggered the majority of rain cells.
- 2) Inside the western corridors, the peak of triggering-point density finely matches specific topographic elements.

A Lagrangian approach limited to the mountainous area, sector 3, was followed to summarize the above observations. The purpose is to compute the mean underlying topography around the triggering point and the corresponding mean rain field. Let us consider the terrain elevation  $H(\mathbf{x})$  known via a DTM; the resolution used is 75 m in the horizontal and 1 m in the vertical. For a set of  $N_t$  triggering points  $x_t$ , the mean underlying topography  $\bar{H}_t$  is defined by

$$\bar{H}_t(X, Y) = \frac{1}{N_t} \sum_{(x_t, y_t) \in D} [H(x_t + X, y_t + Y) - H(x_t, y_t)], \quad (5)$$

where  $(X, Y)$  are the coordinates in a moving window centered on triggering points. Note that the difference

is taken between the altitude of the current point and the altitude of the origin of the window so as to work on relative altitudes.

From a statistical point of view, the raincell position is relief-dependent if the underlying topography  $\bar{H}_t$  differs from the mean topography  $\bar{H}$ , which can be estimated by

$$\bar{H}(X, Y) = \frac{1}{N_D} \sum_{(x, y) \in D} [H(x + X, y + Y) - H(x, y)], \quad (6)$$

where  $N_D$  is the total number of DTM points in the study area.

The difference,  $\delta(X, Y) = \bar{H}_t(X, Y) - \bar{H}(X, Y)$ , between the mean topography conditioned by the presence of a rain cell and the mean topography is mapped in Fig. 15. In this figure, the mean rain field centered on the triggering point is also represented according to the following formula:

$$\bar{R}_t(X, Y) = \frac{1}{N_t} \sum_{(x_t, y_t) \in D} R(x_t + X, y_t + Y). \quad (7)$$

The superimposition of these two maps gives a synthetic view of an orographic rain cell and its underlying topography. Thus, the underlying topography significantly differs from the mean topography. The gradients of the difference between the two fields are on the order of 100 m in 10 km. These differences not only concern the slope but also the shape of the relief. The triggering point is

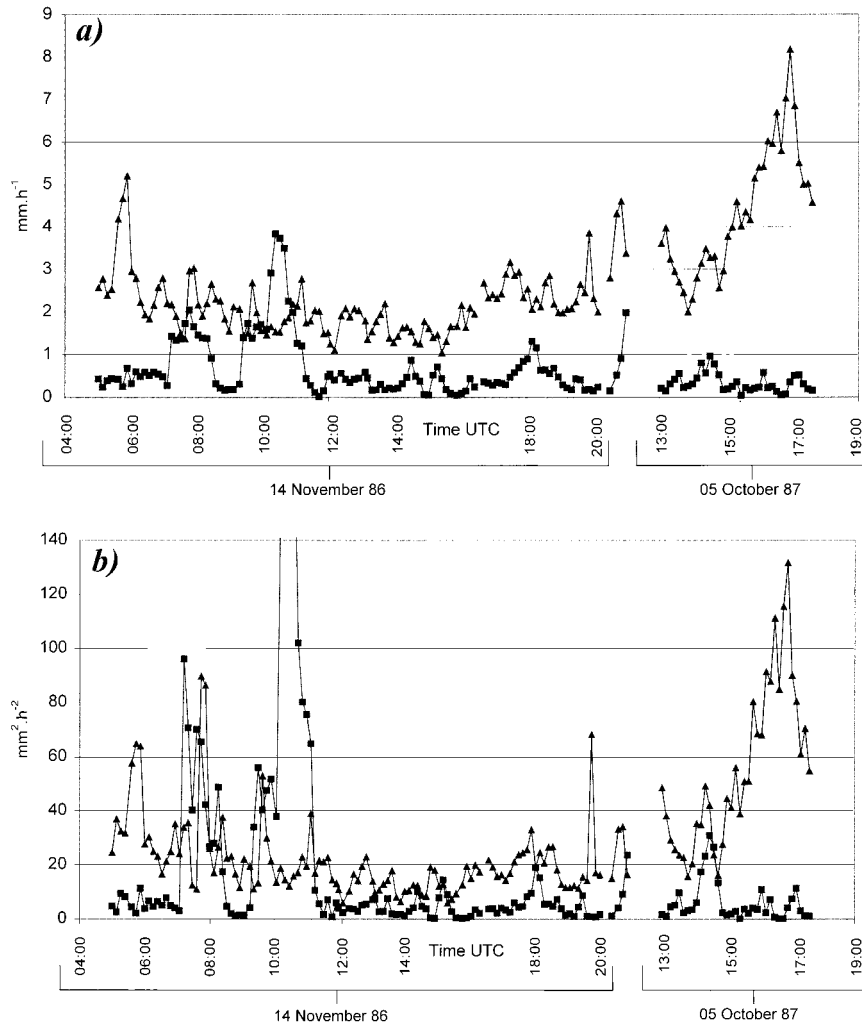


FIG. 16. (a) Time evolution of the (a) mean rain and (b) rain variance over sectors 2 (■) and 3 (▲).

positioned on the southeast flank of a marked shoulder. Moreover, the mean rain field is delineated by north–south-oriented oblate shapes with a slight shift toward the east up to the  $4 \text{ mm h}^{-1}$  contour. It exhibits a marked maximum of  $17 \text{ mm h}^{-1}$  close to the triggering point (2 km north, which gives a mean gradient of  $5 \text{ mm h}^{-1} \text{ km}^{-1}$ ). On average, the highest rain intensities are thus concentrated close to the southern edge of orographic cells, and the rain patterns are slightly deflected toward east according to the general orientation of topography.

The above analysis confirms that the positioning of individual orographic cells with regard to the relief is not random; they are triggered by specific relief features.

## 6. Dynamics of rain inside orographic bands

This section will analyze the rain variability in time. The evolution in time of the first two direct moments and the space–time structure function of rain inside orographic bands are the tools retained for this analysis.

### a. Mean and variance fluctuations in time

Using Eqs. (1) and (2), the mean and variance evolution in time of the rain field are displayed in Figs. 16a,b. For reasons of homogeneity in space, sectors 2 and 3 are considered separately. As expected from the above analysis, the two sectors have significantly different behavior. We must remember from Fig. 7 that the analyzed sequence covers a period of 16 h during which the wind flux is almost stable ( $25 \text{ m s}^{-1}$  at Mont Aigoual) and a period of 4 h during which the wind varies strongly, multiplying its velocity by 1.5. Sector 3, containing the three more-active western bands, has higher and more stable rain intensities (between 2 and  $3 \text{ mm h}^{-1}$  vs less than  $1 \text{ mm h}^{-1}$  for sector 2). The wind velocity is prone to noticeable changes: the mean rain rate roughly doubles within two hours. The dispersion of rain intensities in space is also very stable in time (variance between 60 and  $80 \text{ mm}^2 \text{ h}^{-2}$ ). Sector 2 is less active

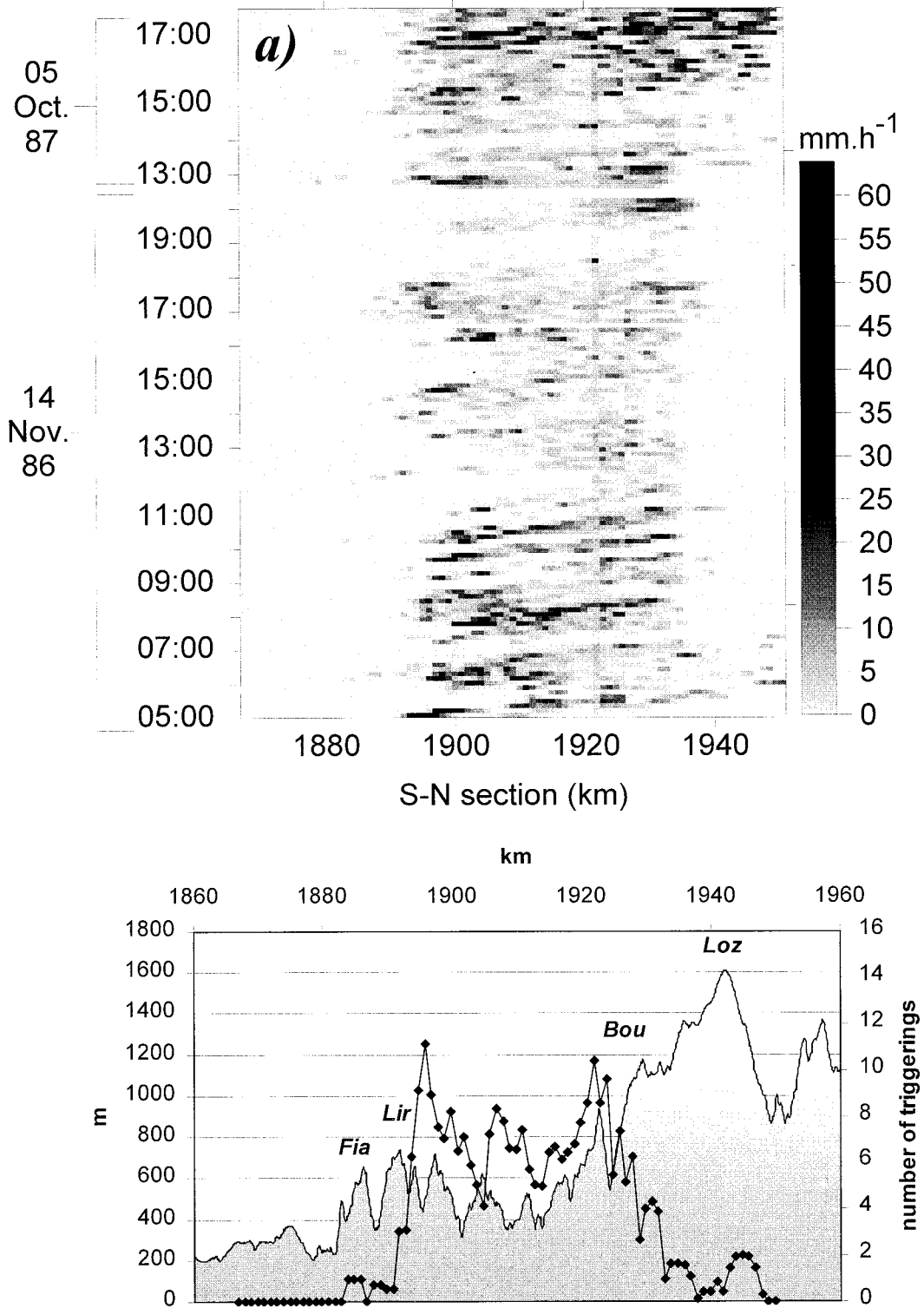


FIG. 17. RTI corresponding to the rainbands at (a)  $X = 718$  km and (b)  $X = 730$  km in sector 3. Missing data are blanked. The related topographic profile is represented in the bottom box with the number of triggerings along the section (diamonds).

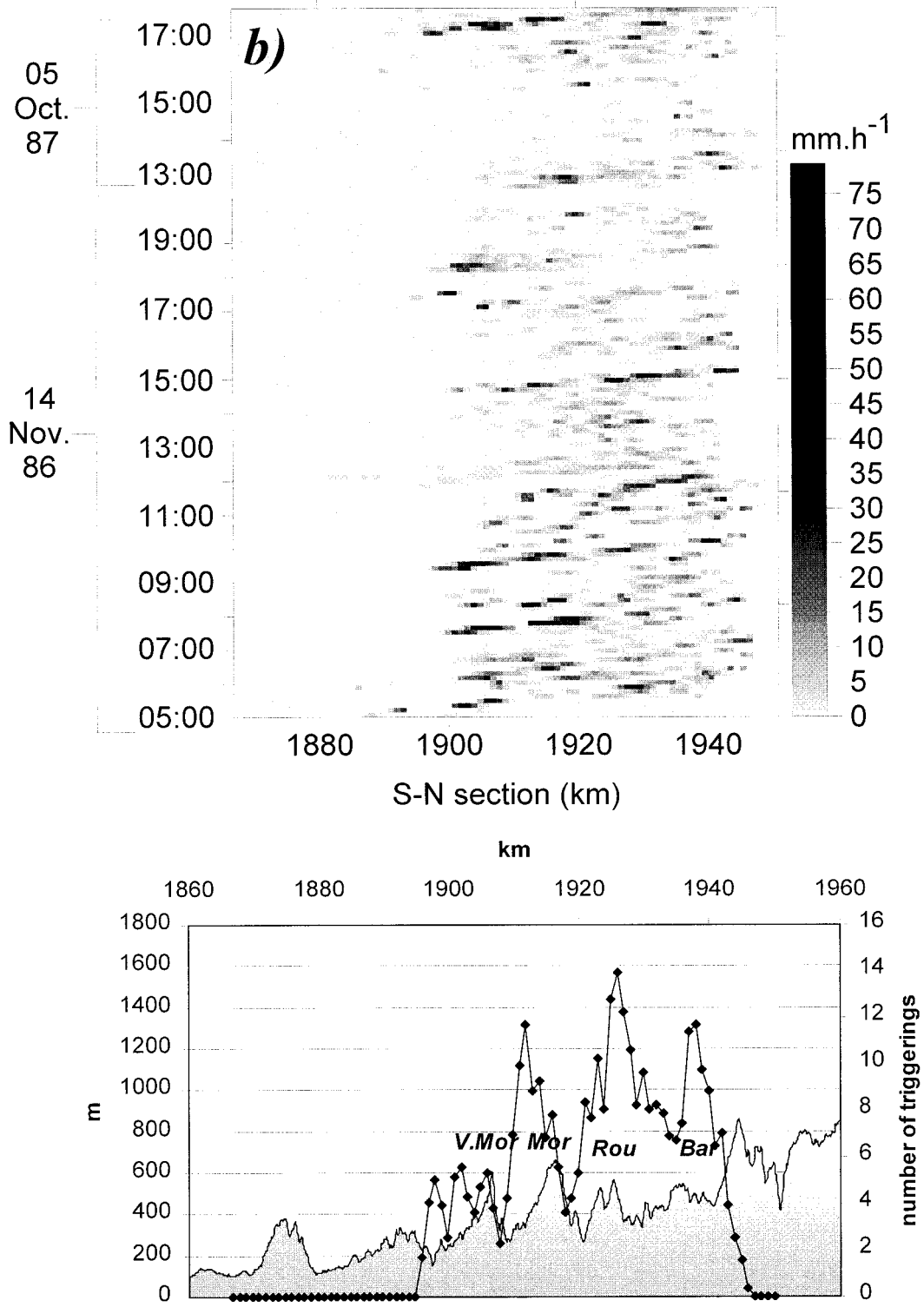


FIG. 17. (Continued)

and less stable (mean around 0.5 mm h<sup>-1</sup>, showing several peaks above 1 mm h<sup>-1</sup>). Rain dispersion is comparable to that of sector 3 and varies much in time. The difference in wind regime is not sensitive.

*b. Space-time structure function*

To analyze rain fluctuations inside the bands the RTI technique is applied. From each successive radar pic-

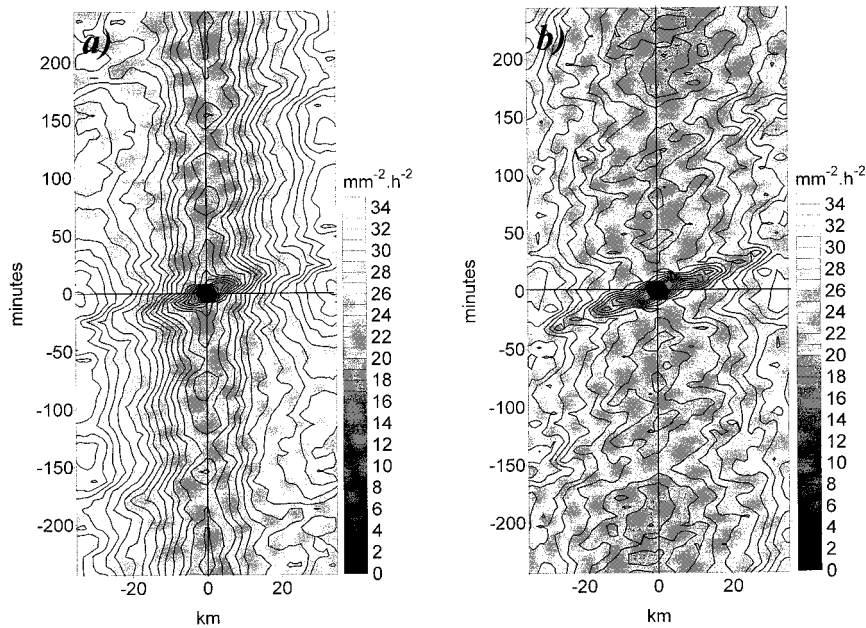


FIG. 18. Two-dimensional variogram maps of RTI calculated for two rainband sections at (a)  $X = 718$  km and (b)  $X = 730$  km.

ture, a north–south section is extracted at a coordinate  $X$  corresponding to the selected band, and these sections are displayed as a function of time. The north–south direction is related to the dominant wind direction. Should the wind have a different direction, the RTI would need to be built differently. For practical reasons, three rows of pixels ( $X \pm 1$  km) are averaged. This limits the number of unavailable data and partially makes up for the irregularities of rain bands.

Figure 17 displays the RTI of two active bands of the mountainous area (sector 3) located at  $X = 718$  km and at  $X = 730$  km. Corresponding topographic profiles are drawn to recall the shape of the underlying relief: the north end of the first band is marked by the presence

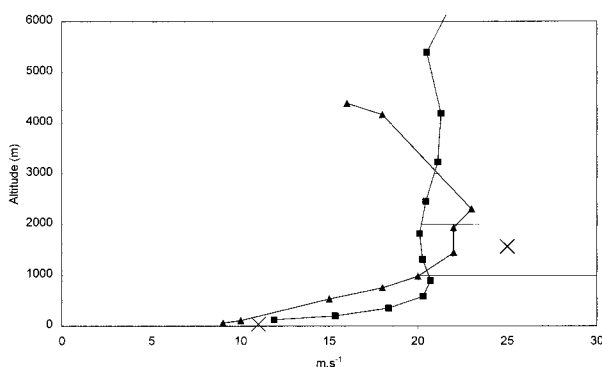


FIG. 19. Vertical profile of wind intensity upstream of the relief from the French Peridot operational meteorological model analyses at 0000 UTC 14 Nov 1986 (■) and sounded at Nîmes weather station at the same time (▲). The wind velocity measured at the ground by the two weather stations of Nîmes and Mont Aigoual is also reported (×).

of Mont Lozère (1600 m), beyond which radar detection is scarce, and the second band covers lower, less-differentiated altitudes. Stable vertical patterns at a given location  $X$  are the signature of some remaining ground clutter not eliminated by the radar data processing (see for example  $X = 1923$  km in Fig. 17a or  $X = 1905$  km in Fig. 17b). Inclined patterns reveal the propagation of rain cells in space. The origin of the different tracks coincides well with the identified triggering points. The size of the rain cells does not exceed a few kilometers. The slope of these inclined patterns corresponds to the propagation speed (approximately  $60 \text{ km h}^{-1}$ ). A pulsation in time of these inclined patterns is also visible.

To synthesize these observations, RTI pictures can be analyzed with the 2D variogram function defined in Eq. (4). The mean quadratic gradient of rain intensities over a moving window features the autocorrelation of the process in time and space. Figure 18 gives the space–time variogram that corresponds to the two selected RTI presented in Fig. 17. The following comments can be made.

- 1) For a fixed time, the variogram shows similar behavior in space with the vertical axis of the space variogram of Fig. 11. The difference comes from the sampling domain, which is restricted in Fig. 18 to the inside of rain bands. The decorrelation length is typically equal to 5–7 km (taking  $15 \text{ mm}^2 \text{ h}^{-2}$  as a limit corresponding to 50% of explained variance).
- 2) Along a fixed position in space, the variogram reveals the autocorrelation of rain intensities in time. The decorrelation time is very short (less than 10 min), but some time periodicity is indicated by regularly-spaced submaximums of the variogram (18

$\text{mm}^2 \text{h}^{-2}$ ; they represent 40% of explained variance). After Fig. 18b, the period is around 40 min. On Fig. 18a, this 40-min period is much less clear and only a double value around 80 min leaves no doubt. When considering the time analysis of these radar data, we must keep in mind that the scanning rate of the radar was only one picture each 8–10 min. This frequency is too low to be sure whether the periodicity of the rain process is different from one band to the other or whether the observed difference is merely caused by the phasing between the radar and the rain process (aliasing effect).

- 3) Inclined patterns highlight the space–time coherence of rain fields caused by the advection of rain cells. The slope of the patterns gives an estimate of the propagation speed of approximately  $60 \text{ km h}^{-1}$ . This speed is lower than the constant wind speed measured at the weather station at Mont Aigoual (1565 m). This value is also smaller than the measured and simulated (French “Peridot” operational meteorological model) wind speed in Nîmes (i.e., the sounding at 0000 UTC 14 November 1986; Fig. 19).

For sector 1 ( $X = 760 \text{ km}$ ), the variogram of RTI shows a general pattern of advection with the same speed but without any periodicity. This sector is remarkable for its relative large variance of rain process (1.5 times greater than in sector 2). It thus confirms the variance pattern presented in Fig. 10b.

## 7. Conclusions

This paper illustrates experimental and statistical evidence under stationary meteorological conditions (wind and humidity) that orographic rainbands, parallel to low-level wind direction and assumed to be the same between 39 m (Nîmes weather station) and 1565 m (Mont Aigoual weather station), can persist during several hours over the relief of a Mediterranean region. Orographic rainbands are more active and more stable over the mountains than over the hilly area. They contain northward-moving rain cells whose velocity is consistent with the wind measured in lower layers. Relief shoulders trigger the rain cells on their southeast flank. Their regular spacing of typically 15 km is responsible for the general organization of the rainbands.

The relationship between rain fields and topography is not straightforward on the time- and space scales considered. The simple correlation coefficient between the mean rain intensity over the selected dataset and topography is only 0.5, which means that only 25% of the variance of rain is explained by the relief. The application of statistical tools to digital pictures (radar and topography) is probably the only way to point out this relationship.

Even if the current case studies are not sufficiently documented from a meteorological viewpoint, it is possible to put forward some state of points about the de-

velopment of the observed precipitation. Despite the close correspondence between the rain-field organization and small-scale topographic features, the Bergeron effect is not obvious because no feeder rain was detected on the wind side of the relief. The low vertical extension of precipitation and the fast-moving active rain cells identifiable inside the bands lead to the conclusion that shallow convection is triggered by the relief. As far as the sensitivity to wind conditions is concerned, the literature reports  $10\text{-m s}^{-1}$  winds at 900 hPa as a minimum for triggering orographic rain and  $30 \text{ m s}^{-1}$  as generating substantial daily accumulations of about 80 mm of rain (Browning 1980). In the cases studied, the production of rain is consistent with these numbers (50 mm of mean daily rainfall over the mountainous area, with  $25 \text{ m s}^{-1}$ ). The data also show that the daily accumulations could increase up to more than 100 mm with higher wind velocities (5 mm of hourly areal rainfall over the hilly area with around  $30 \text{ m s}^{-1}$  wind velocity during the sequence of October 1987). The radar pictures show that these quantities are not homogeneously distributed in space, leading to local totals up to 2 or 3 times the mean value.

A larger dataset would be very welcome to analyze more extensively the conditions of the development of such orographic rain. In particular, it would be interesting to observe whether other low-level flux conditions in terms of wind speed and direction, relative humidity, and temperature are able to produce comparable rain fields. At present, few continuous radar observations are available in medium mountainous regions around the Mediterranean with the exception of the recent dataset collected during the Mesoscale Alpine Program (Binder et al. 1995) experiment located in the Italian Alpine region during the autumn of 1999. Non-hydrostatic cloud numerical modeling will certainly help to address questions on the sensitivity to the flux conditions and could also give more insights about the governing relief scales. In a preliminary study, Cosma et al. (2001) show that a numerical model reproduces the bands when the horizontal resolution is increased up to 1 km. This result stresses the importance of the topography resolution when simulating orographically forced precipitation. The statistical analysis given in this paper should be applied to simulated rain fields.

In terms of climatology, the low-level winds from the south quadrant constitute the main source of orographic rainfall in the study area. The western quadrant is sheltered by the western part of Massif Central range, and the northern and eastern quadrants are hardly prone to these climatic phenomena. Thus the distribution of rain accumulations over long periods is certainly marked by the general structure described in this paper. Despite the development of physically based interpolation techniques of gauge readings, the orographic rain fields are usually presented as smoother than the one presented in this paper.

For the water cycle over these regions, the suggested

splitting of the rain fields into dynamic and static components is significant. It can be thought roughly that lasting orographic rainfalls govern the groundwater component of the hydrologic response and the more dynamic and active patterns of convective and frontal rain stimulate the fast surface component of the response. Nothing precise is known concerning the respective hydrologic impact of these components.

*Acknowledgments.* The authors thank the anonymous reviewers for their suggestions and comments. The current study was performed under the PATOM and PNRH research programs of the CNRS-INSU, the French Institute for the Universe Sciences.

## REFERENCES

- Alpert, P., 1986: Mesoscale indexing of the distribution of orographic precipitation over high mountains. *J. Climate Appl. Meteor.*, **25**, 532–545.
- , and H. Shafir, 1989: Mesoscale distribution of orographic precipitation: Numerical study and comparison with precipitation derived from radar measurements. *J. Appl. Meteor.*, **28**, 1105–1117.
- Amoroch, J., and B. Wu, 1977: Mathematical models for the simulation of cyclonic storm sequences and precipitation fields. *J. Hydrol.*, **32**, 329–345.
- Andrieu, H., and J. D. Creutin, 1995: Identification of vertical profiles of radar reflectivity for hydrological applications using an inverse method. Part I: Formulation. *J. Appl. Meteor.*, **34**, 225–239.
- , —, G. Delrieu, and D. Faure, 1997: Use of a weather radar for the hydrology of a mountainous area. Part I: Radar measurement interpretation. *J. Hydrol.*, **193**, 1–25.
- Austin, P. M., and R. A. Houze, 1972: Analysis of the structure of precipitation patterns in New England. *J. Appl. Meteor.*, **11**, 926–935.
- Banta, R. M., 1990: The role of mountain flows in making clouds. *Atmospheric Processes over Complex Terrain, Meteor. Monogr.*, No. 45, Amer. Meteor. Soc., 173–228.
- Barros, A. P., and D. P. Lettenmaier, 1993: Dynamic modeling of the spatial distribution of precipitation in remote mountainous areas. *Mon. Wea. Rev.*, **121**, 1195–1214.
- , and R. Kuligowski, 1998: Orographic effects during a severe wintertime rainstorm in the Appalachian Mountains. *Mon. Wea. Rev.*, **126**, 2648–2672.
- Bergeron, T., 1965: On the low-level redistribution of atmospheric water caused by orography. *Proc. Int. Conf. on Cloud Physics*, Tokyo, Japan, IAMAP/WMO, 96–100.
- Binder, P., and Coauthors, 1995: Mesoscale Alpine Programme: Design proposal. ETH, 65 pp. [Available from MAP Data Centre, ETH, Zurich, Switzerland.]
- Bougeault, P., and Coauthors, 2001: The MAP special observation period. *Bull. Amer. Meteor. Soc.*, **82**, 433–462.
- Browning, K. A., 1980: Structure, mechanism and prediction of orographically enhanced rain in Britain. *Orographic Effects in Planetary Flows*, World Meteorological Organization, 85–114.
- Chua, S.-H., and R. L. Bras, 1982: Optimal estimators of mean areal precipitations in regions of orographic influence. *J. Hydrol.*, **57**, 23–48.
- Cosma, S., E. Richard, and F. Miniscloux, 2001: The role of small-scale orographic features in the spatial distribution of precipitation. *Quart. J. Roy. Meteor. Soc.*, in press.
- Cotton, W. R., and R. A. Anthes, 1989: *Storm and Cloud Dynamics*. International Geophysics Series, Vol. 44, Academic Press, 883 pp.
- , R. L. George, P. J. Wetzell, and R. L. McAnelly, 1983: A long-lived mesoscale convective complex. Part I: The mountain-generated component. *Mon. Wea. Rev.*, **111**, 1893–1918.
- Creutin, J. D., and C. Obled, 1982: Objective analyses and mapping techniques for rainfall fields: An objective comparison. *Water Resour. Res.*, **18** (2), 413–431.
- , H. Andrieu, and D. Faure, 1997: Use of a weather radar for hydrology of a mountainous area. Part II: Radar measurement validation. *J. Hydrol.*, **193**, 26–44.
- Daly, C., R. P. Neilson, and D. L. Phillips, 1994: A statistical-topographic model for mapping climatological precipitation over mountainous terrain. *J. Appl. Meteor.*, **33**, 140–158.
- Gandin, L. S., 1965: *Objective Analysis of Meteorological Fields*. Israel Program for Scientific Translations, 242 pp.
- Goodison, B. E., B. Sevruk, and S. Klemm, 1989: WMO solid precipitation measurement intercomparison: Objectives, methodology, analysis. Preprints, *IAHS Symp. on Atmospheric Deposition*, Baltimore, MD, IAHS Vol. 179, 57–64.
- Gupta, V. K., and E. C. Waymire, 1979: A stochastic study of subsynoptic space-time rainfall. *Water Resour. Res.*, **15**, 637–644.
- Harimaya, T., and K. Tobizuka, 1988: Enhancement of rainfall by the orographic effect: A case study. *J. Disaster Sci.*, **10**, 13–24.
- Hevesi, J. A., J. D. Istok, and A. L. Flint, 1992a: Precipitation estimation in mountainous terrain using multivariate geostatistics. Part I: Structural analysis. *J. Appl. Meteor.*, **31**, 661–676.
- , A. L. Flint, and J. D. Istok, 1992b: Precipitation estimation in mountainous terrain using multivariate geostatistics. Part II: Isohyetal maps. *J. Appl. Meteor.*, **31**, 677–688.
- Hill, F. F., K. A. Browning, and M. J. Bader, 1981: Radar and rain gauge observations of orographic rain over south Wales. *Quart. J. Roy. Meteor. Soc.*, **107**, 643–670.
- Johnson, G. L., and C. L. Hanson, 1995: Topographic and atmospheric influences on precipitation variability over a mountainous watershed. *J. Appl. Meteor.*, **34**, 68–87.
- Joss, J., and A. Waldvogel, 1990: Precipitation measurement and hydrology. *Radar in Meteorology: Battan Memorial and 40th Anniversary Radar Meteorology Conference*, D. Atlas, Ed., Amer. Meteor. Soc., 577–606.
- Kumar, P., and E. Foufoula-Georgiou, 1993: A multicomponent decomposition of spatial rainfall fields: 1. Segregation of large and small-scale features using wavelet transforms. *Water Resour. Res.*, **29**, 2515–2532.
- Lovejoy, S., and B. B. Mandelbrot, 1985: Fractal properties of rain, and a fractal model. *Tellus*, **37A**, 209–232.
- Matheron, G., 1965: *Les Variables Régionalisées et Leur Estimation (Estimation of the Spatialized Variables)*. Masson, 305 pp.
- Messaoud, M., and Y. B. Pointin, 1990: Small time and space measurements of the mean rainfall rate made by a gage network and by a dual-polarization radar. *J. Appl. Meteor.*, **29**, 830–841.
- Michaud, J. D., B. A. Auvine, and O. C. Penalba, 1995: Spatial and elevational variations of summer rainfall in the southwestern United States. *J. Appl. Meteor.*, **34**, 2689–2703.
- Pointin, Y., D. Ramond, and J. Fournet-Fayard, 1988: Radar differential reflectivity  $Z_{DR}$ : A real-case evaluation of errors induced by antenna characteristics. *J. Atmos. Oceanic Technol.*, **5**, 416–423.
- Rosenfeld, A., 1969: Picture processing by computer. *Computer Science and Applied Mathematics*. Academic Press, 196 pp.
- Schermerhorn, V. P., 1967: Relations between topography and annual precipitation in western Oregon and Washington. *Water Resour. Res.*, **3**, 707–711.
- Sevruk, B., and S. Klemm, 1989: WMO solid precipitation measurement intercomparison: Objectives, methodology, analysis. Preprints, *IAHS Symp. on Atmospheric Deposition*, Baltimore, MD, IAHS Vol. 179, 57–64.
- Smith, J. A., and W. F. Krajewski, 1987: Statistical modeling of space-time rainfall using radar and raingage observations. *Water Resour. Res.*, **23**, 1893–1900.
- Smith, R. B., 1979: The influence of mountains on the atmosphere. *Advances in Geophysics*, Vol. 21, Academic Press., 87–230.
- Zawadski, I. I., 1973: Statistical properties of precipitation patterns. *J. Appl. Meteor.*, **12**, 459–472.